ADVANCES IN CHEMICAL PHYSICS, 2025, Vol. 44, No. 1, pp. 83–93

REACTIONS ON SURFACE

INVESTIGATION OF INTERNAL STRUCTURE AND LOCAL ELASTIC PROPERTIES OF HUMAN HAIR WITH ATOMIC FORCE MICROSCOPY

© 2025 N. A. Erina*

Semenov Federal Research Center for Chemical Physics, Russian Academy of Sciences, Moscow, Russia

**e-mail: natalia.erina@mail.ru*

Received December 25, 2023

Revised January 18, 2024

Accepted January 22, 2024

Abstract. The detailed microstructure of human hair in the transverse and longitudinal directions was studied using of atomic force microscopy (AFM) in the mode of intermittent probe oscillation (known as TappingMode™). In addition, operating in AFM-based nanoindentation the local elastic properties (Young modulus, E_{loc}) were determined in various zones of the hair. For quantitative analysis of E_{loc} precise calibration of the AFM system and assessment of the tip apex geometry were carried out. To calculate the numbers of E_{loc} the adapted Sneddon contact mechanical model was used.

Keywords: *human hair, atomic force microscopy, nanoindentation, keratin, internal structure of hair in longitudinal and transversal sections, local Young modulus in longitudinal and transversal sections*

DOI: 10.31857/S0207401X250111e7

1. INTRODUCTION

Structurally, human hair is a complex hierarchical organization based on keratin – keratinized derivatives of epithelial cells of the skin. Keratins are a family of fibrillar proteins with high mechanical strength. Chemically, hair is composed of 65–95% α-aliphatic amino acids tyrosine, glycine and cysteine, 15–35% water, 1–9% lipids and less than 1% enzymes, pigments and cholesterol. The high content of sulfur-containing cysteine leads to the establishment of disulfide bonds between neighboring keratin chains, forming cysteine units. Along with disulfide bonds, the hair structure contains many peptide bonds containing numerous –CO and –NH groups that form hydrogen bonds between neighboring protein fibers. The resulting cross-linked keratin structure is responsible for the shape, structure and strength of the hair fibers [1]. It has been found that the chemical composition of hair can vary depending on the origin, sex, age and other conditions of the organism.

The hair consists of three morphological regions: the outer (cuticle), cortical (cortex), and core (medulla) (Fig. 1a). The cuticle is the outer protective sheath of the hair shaft, which is a keratinized nucleusless cells arranged in the form of scales forming a characteristic pattern and composed of a protein substance containing keratin and sulfur.

The structure of the cuticle is complex and is divided into several functional sub-layers: epicuticle, *A*-layer, exocuticle and endocuticle. Organic components of the cuticle (lipids, proteins and wax-like substances) provide hair with elasticity and natural shine. When the cuticle is damaged, its outer cells die and begin to peel off, and the hair surface loses its smoothness and healthy appearance [2].

The middle part of the hair (cortex) occupies up to 80% of the volume of the hair shaft and determines to the greatest extent the complex of its mechanical properties. The cortex is built of long, densely packed cells of different types (para- and ortho-) of spiral shape, connected by intercellular substance. The paracortical cells have a uniform shape and are only found in straight hair, while due to the orthocortical inhomogeneous cells, the hair is curly. Each cortex cell consists of bundles of keratin protofibrils, successively forming micro- and then macrofibrils oriented along the main axis of the hair [3]. In addition, it has been established that it is the cortex that contains the pigment melanin, which determines hair color [4].

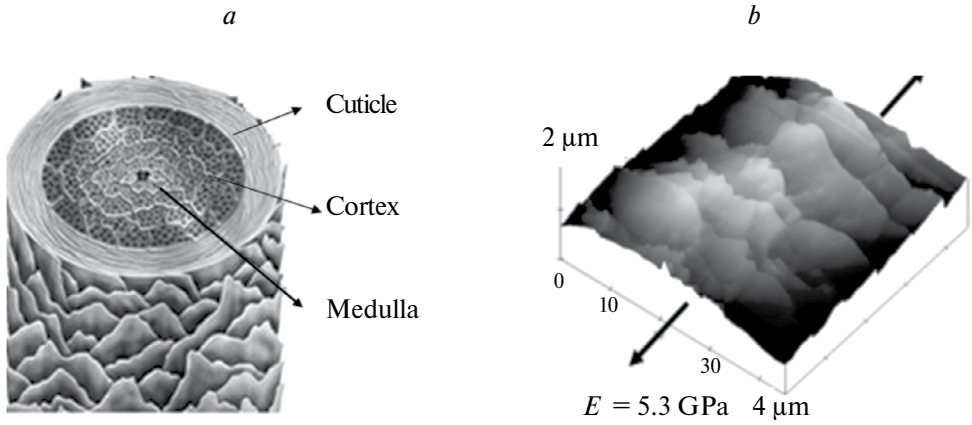

Fig. 1. *a* – Schematic image of the internal structure of the hair [saylordotorg.github.io]. *b* – Three-dimensional topographic image of the outer layer of the hair, obtained on a scanning probe microscope MultiMode™ (Bruker NanoSurface Inc., USA) in the oscillation mode (Tapping Mode™). The Young's modulus of the hair in uniaxial tension was determined on an Instron-3365 tensile testing machine (UK)

The innermost layer of the hair shaft (medulla) is a loosely packed channel of proteinaceous non-corneal cells in the central part of the hair, which may be continuous or fragmented. It has been suggested that the medulla is part of the excretory system of the hair and contains heavy metals and traces of drugs [2].

Hair consists of 80–90% keratin. The remaining substances are mainly water (for elasticity) and lipids (for protection). In essence, the hair shaft is different types of keratin assembled into differently shaped elements that are bound together by keratin-like cement [2]. As early as 1951, using X-ray and protein modeling experiments considering bond lengths and valence angles, it was shown that the fibrillar material of hair consists of spiral-shaped α-keratin fibers [5]. It has also been suggested that there is another form of keratin assembly in the form of folded plates of *β-keratin* that can be reversibly stretched to approximately 100% elongation (Fig. 2) [6]. Such an extremely complex structure provides high mechanical properties of the hair.

A large number of studies on natural wool fibers have been conducted to establish the relationship between the fine texture of the microfibril matrix and the macroscopic properties of the fiber. The molecular mechanism of microfibril deformation has been described as a gradual transition from α-helical tufts to β-layered structures [7]. Using this mechanism as the main mechanism, attempts have been made to explain the elastic response of keratin fibers in terms of its two structural subcomponents [8]. The value of the elastic modulus (Young's modulus) can vary from 2 to 8 GPa depending on the ethnicity, gender and age of the individual. The tensile strength ranges from 200 to 300 MPa, which is equivalent to that of lead, copper or platinum and comparable to that of steel [4, 9].

Currently, scanning probe microscopy (SPM) [10], which includes several methodological approaches, is widely used to obtain structural information of various materials: tunneling probe microscopy, which allows obtaining information on the topography and electrical characteristics of electrically conductive materials [11–14] and atomic force microscopy (AFM) [15].

AFM has made it possible to extend the scope of application of the SPM method to a wide range of materials by recording various forces of interatomic interaction between the probe and the sample surface. The basic principle of AFM is to record various forces of interaction (attraction or repulsion) between the probe located at the end of an elastic microcantilever (cantilever) and the surface of the sample [16]. Unlike the widely used electron and transmission electron microscopy, which require special techniques for surface preparation and contrasting of sample components, AFM is not an invasive methodology. In addition, AFM allows to simultaneously investigate topography, structural features and probe local physical and mechanical properties (elasticity, adhesion, electro-magnetic characteristics) of a wide range of materials with high spatial resolution [17].

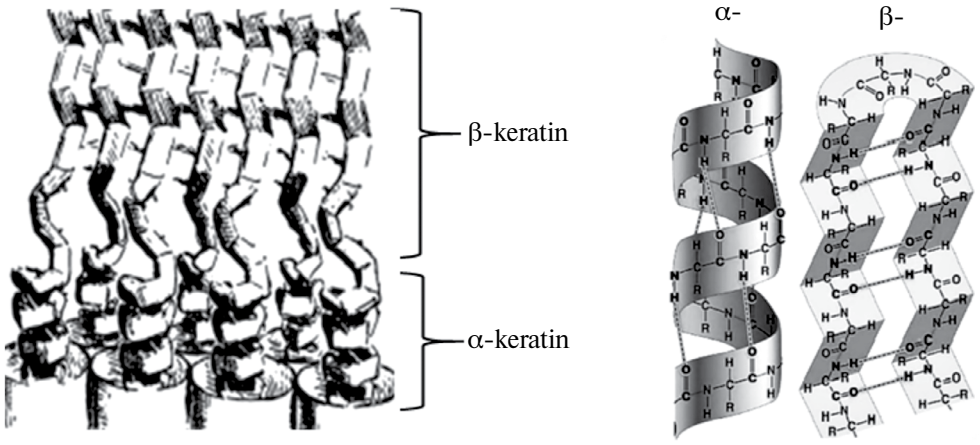

Fig. 2. Illustration of the packing of spiral-shaped ensembles of α-keratin that transform into folded plates of β-keratin when stretched

A key step in the development of AFM applications was the development of an oscillating mode (or intermittent contact) called TappingMode™ [18]. In this mode, the probe interacts with the sample surface for a very short period of time, which minimizes the influence of lateral friction forces during scanning and allows the examination of very soft samples without damaging their surface. At the beginning of the procedure, an elastic beam (cantilever) with a probe at the end is driven into free oscillation in the vertical direction at its resonant frequency and corresponding amplitude by means of a piezo element. The damping of the amplitude due to the resulting attraction forces between the probe and the sample is the mechanism for generating the surface topography. At the same time, a so-called phase image is mapped, the contrast change on which is caused by the shift of the phase angle of oscillations when the probe interacts with material regions having different mechanical properties. As a rule, a brighter contrast on the phase image corresponds to the most rigid and less dissipative regions of the material. However, one cannot quantitatively extract any specific mechanical characteristic of the material from the phase contrast, since the phase shift of the cantilever oscillations is due to the convolution of elastic, adhesive, and dissipative contributions at the moment of probe-sample contact [19].

Indentation [20] has become a theoretically and experimentally confirmed method for quantitative determination of local physical and mechanical properties of materials, including the application of the AFM methodology called nanoindentation [21]. This method of testing materials is based on indentation of the indenter into the specimen and recording, so-called force curves (FC), representing the dependence of the indentation depth (H) on the applied load (F) (Fig. 3).

The loading curve reflects the work expended to overcome the resistance of the material, determined by its stiffness (hardness) when the indenter is pushed in. The reverse process of unloading is the work expended to restore the material. In many cases, deformation occurs with the development of plasticity, when the recovery is not elastic, but with a delay due to the presence of structural elements of different viscosity in the material. This leads to energy loss (dissipation) during the unloading cycle and is manifested on the SC as the difference between

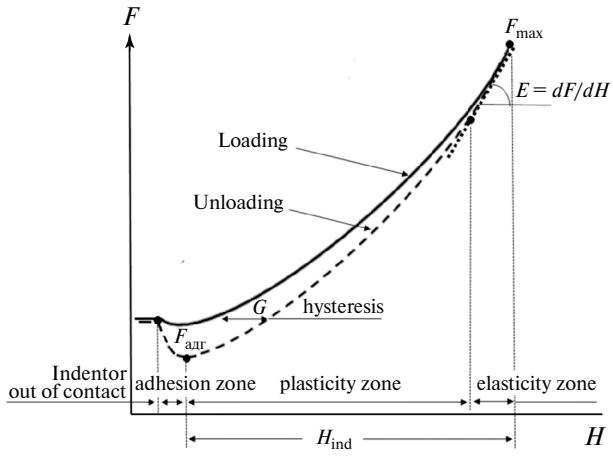

Fig. 3. Conditional force curve obtained by nanoindentation method

the loading and unloading curves, or hysteresis. Therefore, to calculate the modulus of elasticity (E), only the upper straight section of the unloading curve is analyzed by the tangent of its slope, where the material responds elastically in response to the applied force (F_{max}) and the influence of adhesion forces is minimal and hysteresis is not yet manifested.

At the same time, an adequate interpretation of AFM data and their subsequent use for characterizing local mechanical properties of materials requires a good understanding of the effects of probe-sample interactions. There are many contact models for determining the hardness and elasticity of materials during an indentation. One popular approach in this area is based on the Sneddon solution, which relates load to strain and the generated contact area to determine the shape coefficients of various axisymmetric indenters (cylinder, cone, ball, and paraboloid of rotation) [21].

Nanoindentation has been used to perform studies regarding structural mapping and probing of elastic and plastic properties of hair, however, mainly at the qualitative level [22–25]. However, for quantitative extraction of the mechanical characteristics of the material, it is necessary to perform an accurate calibration of the AFM system parameters, determine the stiffness of the cantilever and rationally select and digitize the probe shape.

The purpose of this study is to demonstrate the capabilities of AFM in the study of topography, microstructure and measurement of quantitative local elastic properties (Young's modulus) of human hair in transverse and longitudinal directions with accurate calibration of the AFM system. The variety of mechanical actions on the probe side gives a wide choice for hardware realization.

2. EXPERIMENT

Before the study, a sample of Caucasian human hair (purchased from https://haircenters.ru) was thoroughly washed in deionized water and dried at room temperature. After that, the hair fragments were impregnated in epoxy resin and after its curing were dissected transversely and longitudinally with a diamond knife at room temperature using a MicroStar 01 microtome (Microstar Technology, USA).

AFM studies were performed at room temperature using a MultiMode™ atomic force microscope and a Nanoscope IIIA™ controller from Bruker NanoSurface Inc. (USA). Before the nanoindentation procedure in order to select the most morphologically informative site, structural studies of the samples in the Tapping Mode™ were performed.

To probe the local elastic properties of the material using the nanoindentation method, force curves (FC) were generated to record the forces of attraction and repulsion between the indenter and the surface of the investigated sample (Fig. 3). The modulus of elasticity (Young's modulus) E_{loc} was determined by the slope of the tangent to the initial linear section of the unloading curve.

In order to measure E_{loc} on a quantitative level, a complete calibration of the system was carried out. The stiffness of cantilevers was determined through the procedure of thermal excitation of free oscillations using the built-in SPM-system from the company "PolyTec" (Germany). The obtained stiffness values were in the range from 50–53 N/m. The cantilevers with probes of symmetrical parabolic shape with radius of curvature 30–50 nm with wear-resistant silicon carbide coating from "TeamNanotec GmBH" (Germany) were used. The choice of such probes was due to the possibility of more accurate characterization of their apex geometry. Probe geometry was assessed using SEM-micrographs followed by a piecewise linear interpolation procedure (Fig. 4).

The values of E_{loc} were calculated using LabVIEW program within the framework of Sneddon's contact mechanical model [22]:

$$H(a) = \int_0^1 \frac{f'(x)dx}{(1-x^2)^{1/2}},$$

$$kD(a,E) = \frac{2Ea}{(1-\nu^2)} \int_0^1 \frac{x^2 f'(x)dx}{(1-x^2)^{1/2}},$$

where: *H is* the indentation depth; *a* is the probe-sample contact radius; *E* is the sample modulus of elasticity; *v* is the Poisson's ratio of the sample; *k* is the cantilever stiffness; *D(a, E)* is the cantilever bending during indentation; *f' (x) = w(ax),* where *w* is the coefficient describing the geometry of the probe apex, equal to 1.5 for a paraboloid of rotation. The details of the probe geometry estimation and E_{loc} calculation using the adapted Sneddon model minus the hysteresis contribution are presented in [27].

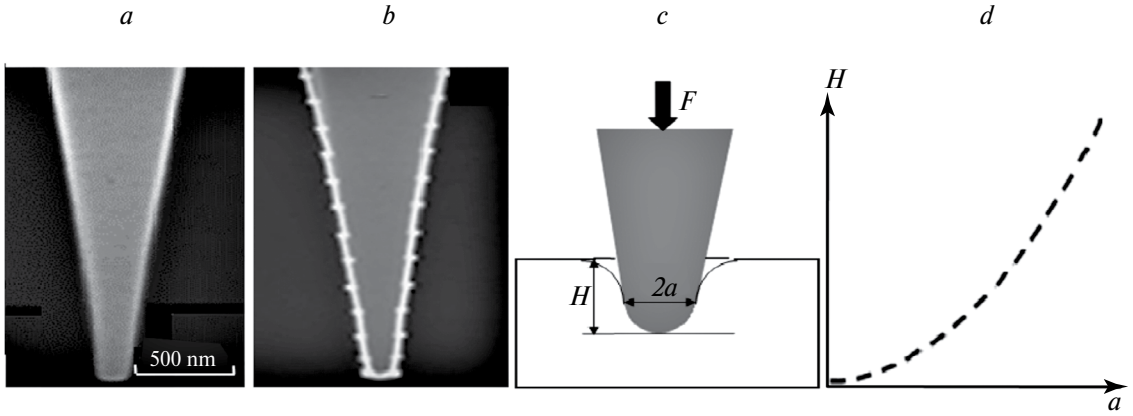

Fig. 4. Estimation of the probe geometry using the piecewise linear interpolation method. *a* – SEM-micrograph of the parabolic probe; *b* – Profile of the probe through a set of rectilinear segments; *c* – Scheme of the probe indentation into the sample surface; *d* – Graph of the function *H(a)* determining the radius of the probe contact with the hypothetical sample at any current indentation depth

3. DISCUSSION OF RESULTS

3.1. Cross section

3.1.1. Structure

Figure 5a shows an optical photograph of a cross-sectional microtomized hair impregnated in epoxy resin. The AFM topographic image of a cross section including the outer cuticular zone and part of the adjacent right cortex zone is shown in Fig. 5b. The cuticle is an ensemble of parallel oriented sublayers, a detailed image of which is shown in Fig. 5 (c, d). Each sublayer (450–600 nm wide) is tightly connected with the neighboring one, forming the so-called membrane complex. As noted above, the main structural elements of each membrane are the so-called A-layer, exocuticle and endocuticle. According to [9] the outer A-layer is a component with a high cysteine content (>30%). It is highly cross-linked and tightly binds neighboring protein layers via disulfide bonds, which provides significant mechanical strength, chemical resistance and low swelling of hair in water. The exocuticle immediately adjacent to the A-layer contains ~15% cysteine, while the endocuticular layer contains only ~3% cysteine [28]. The topographic image in Fig. 5c shows that the exocuticular cells are 150–200 nm wide deepened and the endocuticular layer cells are elevated by ~13 nm and their width is 300–400 nm. In [29], endocuticular cells were found to be more friable due to lower cross-linking sulfur content. This conclusion is supported by the phase image in Fig. 5g, where a less dense (porous) packing of the material is visualized.

The most voluminous part – the cortex – structurally represents irregularly shaped domains with a transverse size from 0.2 to 2.0 μm (Fig. 5 e, f). In contrast to the cuticle, it is in the cortex that rounded-shaped inclusions with a diameter of~ 100 nm are visible, which appear to be particles of melanin pigment that determines hair color (Fig. 5e, f). In addition, the detailed phase image (Fig. 5e) clearly shows that a single subdomain of the cortex is surrounded by a light in contrast chain-like border. The latter is probably the so-called S-border formed by transverse disulfide cross-links, which provide high mechanical strength and elasticity of the hair.

3.1.2. Nanoindentation

Figure 6a shows a topographic image of the cuticular zone of the hair with traces left after the nanoindentation procedure. It can be seen that indents in the elevated exocuticular zones are clearly visualized and have a much larger diameter than indents in the endocuticular layers. This fact correlates with the above-mentioned statement about a denser degree of cross-linking and corresponds to the data of [29]. In addition, around the indents in the exocuticular layers, light contrast framing is visible, indicating a more pronounced irreversible plastic deformation (G) developed during nanoindentation. This conclusion is confirmed by the characteristic force curves for both zones (Fig. 6b, c). It can be seen that the plastic deformation in the stiffer zones is almost 2 times smaller than in the more pliable zones. The averaged values of E_{loc} determined from the slope of the unloading curve in its initial zone using the modified Sneddon equation are: 6.1 ± 0.6 GPa for the stiffer endolayer and 3.9 ± 0.7 GPa for the exolayer.

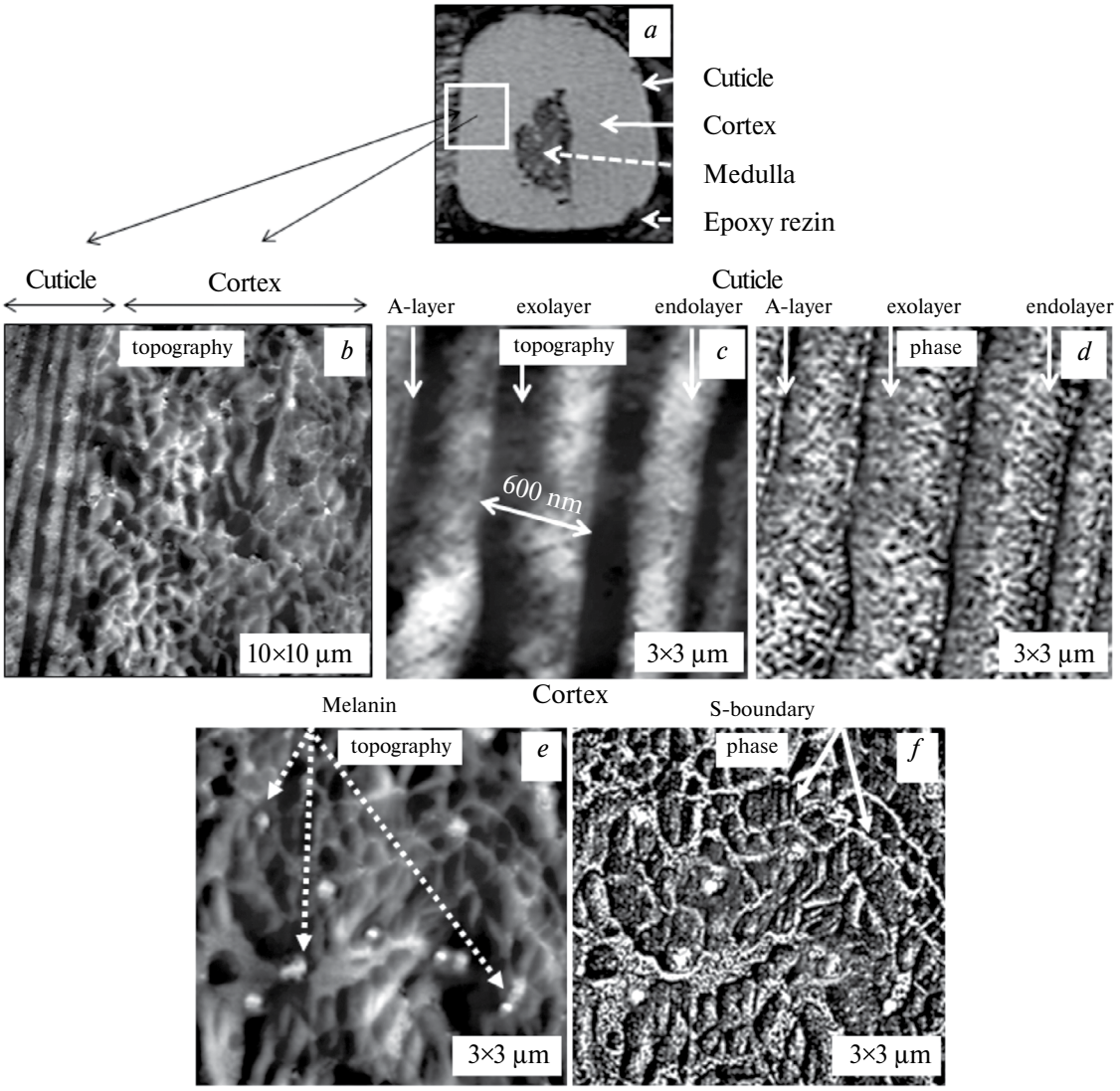

Fig. 5. Features of the internal structure of the hair in perpendicular section. *a* – Optical image of microtomized hair impregnated in epoxy resin. *b* – Topographic image of the outer cuticular zone (left) and part of the cortex zone (right). *c, d* – Detailed topographic and phase images of the cuticle. *e, f* – Detailed topographic and phase images of the cortex

Figure 7 illustrates a topographic image of the cortex zone in the transverse direction with traces of indents and force curves obtained in characteristic structural regions. Three regions can be distinguished, where diameter and depth of indents, as well as local elastic modulus differ markedly (Fig. 7b – d). The variation of the elasticity index in the cortex matrix is probably related to the presence of functionally different cortical cells (para- and ortho-), which differ in the degree of cysteine cross-linking and the density of fibril twisting. Straight hair contains mainly paracortical cells, while curly hair is enriched with orthocortical cells. In our experiment, the paracortical regions of the cortex are 2.5 times stiffer than the orthocortical regions (highlighted by a rectangle): $E_{loc\ para-} = 7.8 \pm 0.5$ GPa (Fig. 7b) vs. $E_{loc\ ortho-} = 2.8 \pm 0.6$ GPa (Fig. 7c). At melanin pigment localization sites (highlighted by circles in Fig. 7d), $E_{loc\ melanin} = 0.9 \pm 0.4$ GPa.

3.2. Longitudinal section

3.2.1. Structure

Figure 8a shows an optical photograph of a longitudinally microtomized hair impregnated in epoxy resin. AFM topographic image of the conjugated zones of cuticle and cortex in the longitudinal direction is shown in Fig. 8b, c. Comparing the structural features in transverse and longitudinal directions

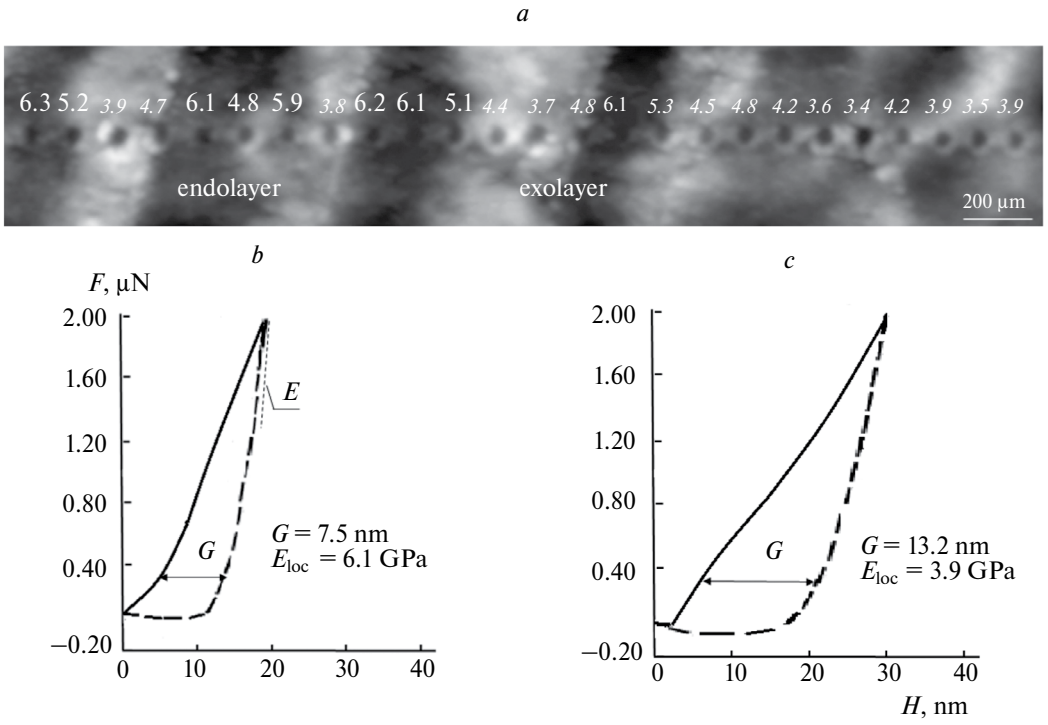

Fig. 6. *a* – Topographic image of the cuticle showing indentation marks and indices of local Young's modulus values for the endo- and exolayer. *b, c* – Characteristic force curves

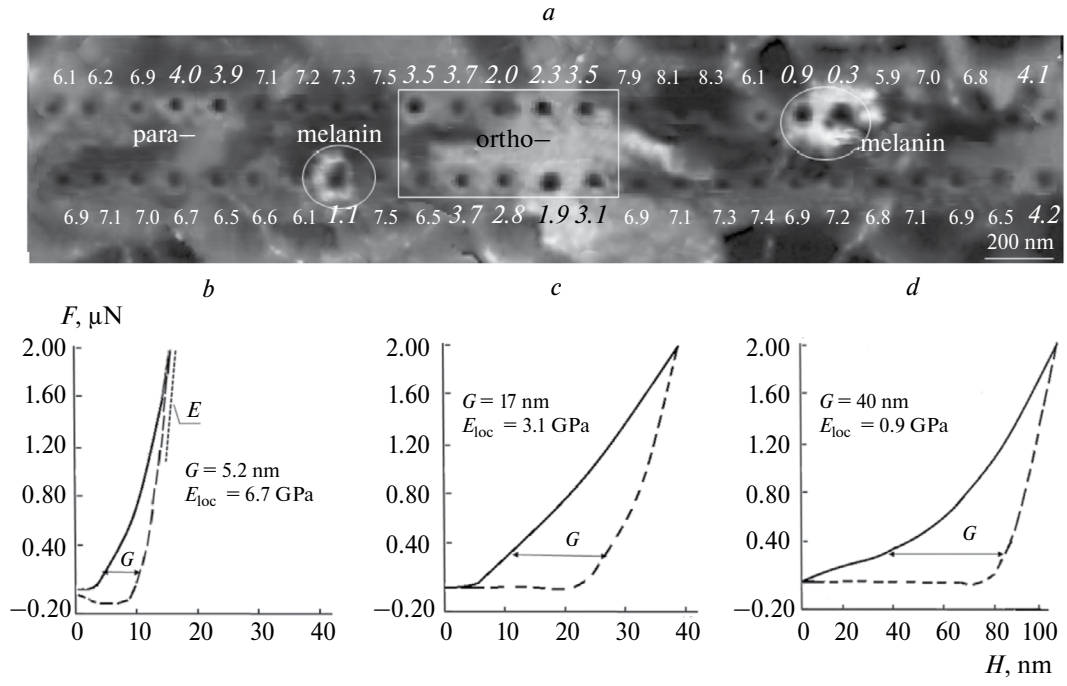

Fig. 7. *a* – Topographic image of the cortex with indentation traces and indices of local Young's modulus values. *b-d* – Characteristic force curves in different zones of the cortex

(Fig. 5a vs. Fig. 8a), one can see the obvious manifestation of morphological anisotropy in both cuticle and cortical areas. It should also be noted that the spiral-shaped structure of the hair cuticle obtained by AFM visually coincides with the α-keratin image predicted by Pauling and Corey using the X-ray method (Fig. 2) [5]. Figure 8c shows that the width of a single twisted cuticle cell is about 600 nm.

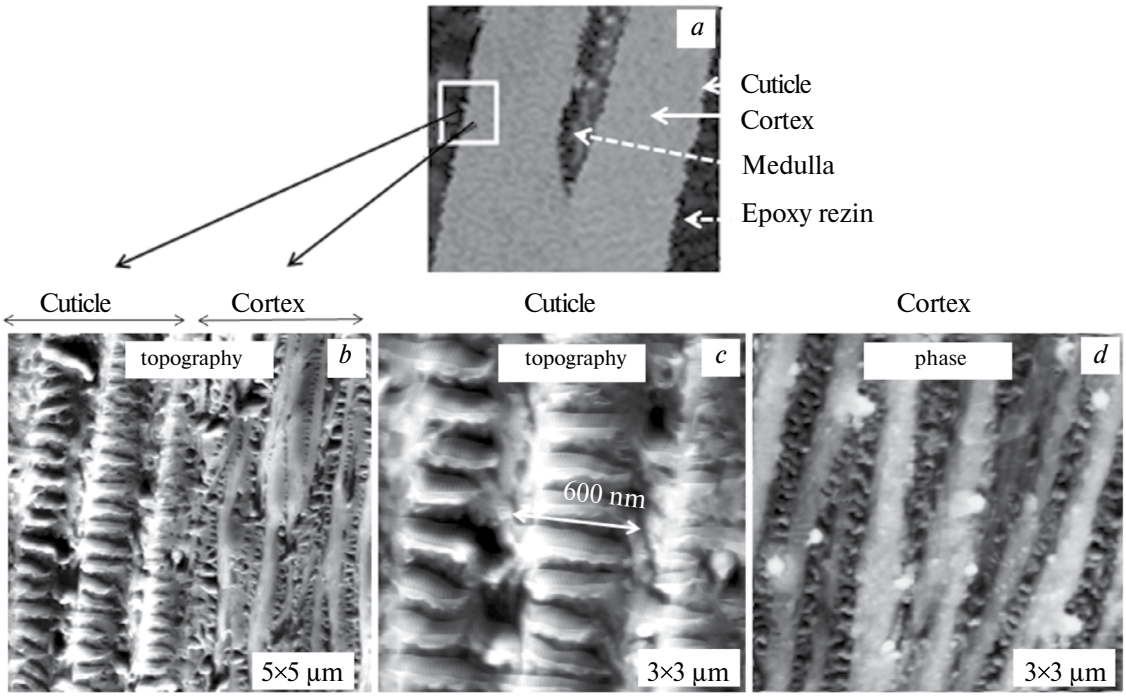

Fig. 8. Features of internal structure of hair in longitudinal section. *a* – Optical image of microtomized hair impregnated in epoxy resin; *b* – AFM topographic image of substructures in conjugated areas of cuticle and cortex *c, d* – Magnified topographic images of cuticle and cortex areas, respectively

Figure 8g illustrates the topography of the cortex, which shows elongated fibers (filaments) of various widths from 70 to 180 nm located along the hair. According to [30] the organization of these filaments is an ensemble of hierarchically organized α-helices. Small clusters of three protofibrils twisted together then twist into nine, forming a kind of "cable" known as a microfibril, which is embedded in an amorphous protein-rich matrix. The hundreds of microfibrils are then organized into a fibrous bundle called polypeptide macrofibrils.

The topographic image (Fig. 8d) also shows that polypeptide marcofibrils are connected in the perpendicular direction by ~15 nm wide ties. These ties are probably cysteine bridges with disulfide bonds involved in the elastic stretching mechanism of the hair. In addition, Fig. 8g visualizes light inclusions of rounded shape with a transverse size of 80–100 nm, which are probably inclusions of melanin pigment.

3.2.2. Nanoindentation

Structural anisotropy is also manifested in the difference of the elastic response in mutually perpendicular sections of the hair. Fig. 9a shows a topographic map of the cuticular zone in the longitudinal direction with localization of the locations where nanoindentation was performed.

It can be seen that, in contrast to previous cases, no indentation marks are observed. This is explained by the fact that the cuticular cell in the direction perpendicular to the helix turn behaves elastically during indentation, demonstrating the effect of rapid restoration of the original shape of the material after applied loading without development or with a small manifestation of hysteresis (Fig. 9b, c). The averaged local Young's modulus in these zones is $E_{loc} = 9.2 \pm 0.7$ GPa. The white points ($E_{loc} = 7.3 \pm 0.4$ GPa) correspond to the location of indents that fell outside the main plane of the helical link. In dark contrast zones, located between neighboring turns of the helix, SCs were not produced due to a large height difference (~ 100 nm).

Figure 10a illustrates the topography of the longitudinal section of the cortex zone with indentation traces and local Young's modulus values. In this zone, we were only able to obtain force curves in the monolithic keratin regions located along the main axis of the hair, where the average local Young's modulus was found to be $E_{loc} = 4.2 \pm 0.4$ GPa. However, force curves that

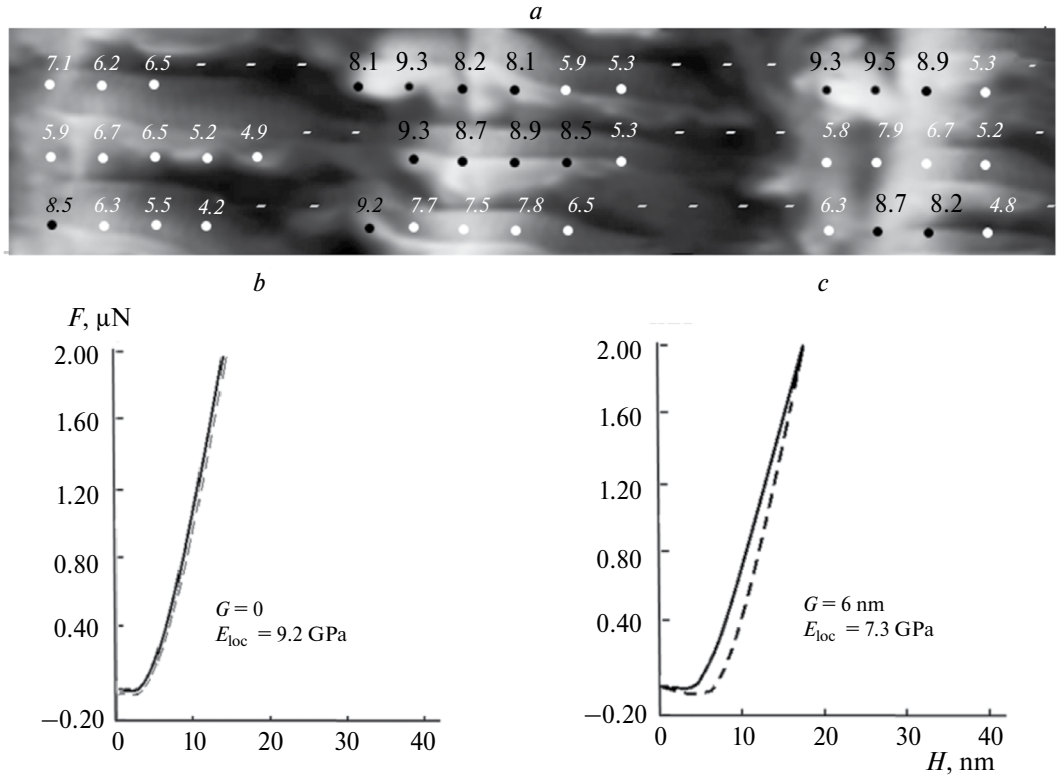

Fig. 9. *a* – Topographic image of the internal structure of the cuticle in the longitudinal direction with indentation of indents location and indices of local Young's modulus values. *b, c* – Characteristic force curves in different zones of the cuticle

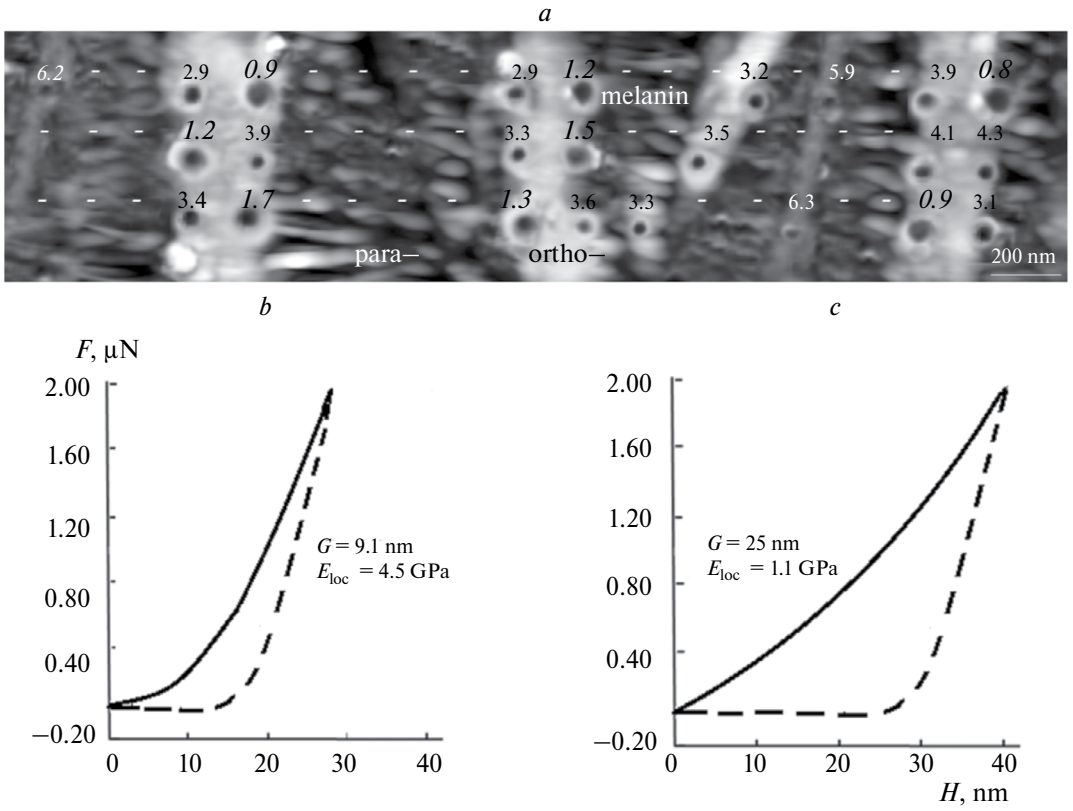

Fig. 10. *a* – Topographic image of the cortex in the longitudinal direction with indentation of indents location and indices of local Young's modulus values. *b, c* – Characteristic force curves in different cuticle zones.

could be taken into account were not reproducibly produced in the darker contrasting (lower) regions. This was probably due to the probe being snagged by transverse disulfide binding ties during extraction from the material, and the initial slope of the unloading curve was not reliably reconstructed. The modulus of elasticity at melanin localization sites was $E_{loc\ mel} = 1.0 \pm 0.3$ GPa.

It should also be noted that the accuracy of the modulus measurement results is affected both by height differences between different morphological elements on the topographic map and by the ratio between the geometric dimensions of structural units and the probe tip. When the linear size of a structural unit is smaller than the size of the contacting probe, the so-called convolution effect – overlapping of the measured structure by the probe – appears. In such situations, the measured values will differ from the true values, which affects the value of statistical scatter.

4. CONCLUSION

The features of the internal structure of the main functional zones (cuticle and cortex) of the native human hair microtomized in transverse and longitudinal directions have been characterized in detail using the AFM method. It is these morphologically complexly organized areas that determine the strength, elasticity and color of hair. It is demonstrated that the hair microstructure is characterized by pronounced structural anisotropy in both morphological zones.

In addition, the local Young's modulus in each structural element was quantitatively measured using AFM nanoindentation. In order to quantitatively measure the local Young's modulus, a preliminary procedure was carried out to fully calibrate the AFM system. The calibration included the steps of measuring the system sensitivity, determining the cantilever stiffness, and estimating the probe apex geometry using TEM followed by a piecewise linear interpolation procedure. An adapted Sneddon model using static analysis was used to calculate Young's modulus.

The nanoindentation method was used to quantify the local elastic modulus in all structurally different regions of the sample, which is not possible in macroscopic studies when generalized integral information is collected for the entire volume of the material under study. The nanoindentation experiment showed that it is the cuticle with densely packed spiral bundles of α-keratin, despite its smaller volume fraction compared to the cortex zone, that determines the elastic properties of the hair.

In the next stage of the study, the structure and measured local elastic properties of hair from the same batch after chemical treatment procedures are expected to be studied using similar techniques.

ACKNOWLEDGEMENTS

The author is grateful to Bruker NanoSurface Inc. (USA) for the opportunity to work on the MultiMode™ AFM microscope.

CONFLICT OF INTERESTS

The author declares that he has no conflict of interest with any party.

ETHICS DECLARATION

This article does not contain any studies using animals as subjects.

REFERENCES

1. *Robbins C. R.*. Chemical and Physical Behavior of Human Hair. N. Y.: Springer, 1988.
2. *Fernandes C., Medronho B., Alves L., Rasteiro M.* // Polymers. 2023. Vol. 15. No. 3. P. 603. https://doi.org/10.3390/polym15030608
3. *Chen N., Bhushan B.* // J. Microscopy. Microscopy. 2005. Vol. 220. P. 96. https://doi.org/10.1111/j.1365–2818.2005.01517.x
4. *Araujo R., Fernandes M., Cavaco-Paulo A., Gomes A.* // Adv. Biochem. Eng./Biotechnol. 2010. Vol. 125. https://doi.org/10.1007/10_2010_88
5. *Pauling L., Corey R. B., Branson H. R.* // Proc. Nat. Acad. Sci. 1951. Vol. 37. No. 4. https://doi.org/10.1073/pnas.37.4.205
6. *Brill R.* //Anal. Chim. 1923. Vol. 434. P. 204.
7. *Feughelman, M.* // Text. Res. J. 1959. P. 223.
8. *Bendit E. G.* // Ibid. 1960. Vol. 30. P. 547.
9. *Mkentane K.* PhD Thesis. Department of Medicine (Trichology & Cosmetic Science). University of Cape Town, 2016.
10. *Binnig G., Rohrer H., Berber C.* // Appl. Phys. Lett. 1981. Vol. 40. No. 2. P. 178.
11. *Grishin M. V., Gatin A. K., Sarvady S. Yu. et al.* // Chemical Physics. 2020. Vol. 39. No. 7. P. 63. https://doi.org/10.31857/S0207401X20070067
12. *Gatin A. K., Sarvadiy S. Yu., Dokhlikova N. V., Grishin M. V.* // Chem. Physics. 2021. Vol. 40. No. 6. C. 10.

https://doi.org/10.31857/S0207401X21060042
13. *Grishin M. V., Gatin A. K., Slutsky V. G., et al.* // Chem. Physics. 2022. Vol. 41. No. 1. P. 3. https://doi.org/10.31857/S0207401X22060048
14. *Grishin M. V., Gatin A. K., Slutsky V. G. et al.* // Chem. Physics. 2023. Vol. 42. No. 1. P. 3. https://doi.org/10.31857/S0207401X23010053
15. *Binnig G., Quate C. F., Gerber. Ch.* // Phys. Rev. Lett. 1986. Vol. 56(9). P. 930. https://doi.org/10.1103/PhysRevLett.56.930
16. *Magonov S. N.* Atomic Force Microscopy in Analysis of Polymers. In Encyclopedia of Analytical Chemistry. / Ed. Meyers R. M. Chichester: John Willey & Sons Ltd, 2000. https://doi.org/10.1002/9780470027318.a2003
17. *Pittenger B., Erina N. A., Su C.* Nanomechanical Analysis of High Performance Materials. Dordrecht: Springer, 2014. https://doi.org/10.1007/978–94–007–6919–9_2.
18. *Zhong Q., Innis D., Kjoller K., Elings V.* // Surf. Sci. Lett. 1993. Vol. 290. No. 7. P. 1688.
19. *Sahin O., Magonov S., Su C., Quate C. F., Solgard O.* // Nature Nanotechnol. 2007. Vol. 2. No. 8. P. 507 https://doi.org/10.1038/nnano.2007.226
20. *Weisenhorn A. L., Hansma P. K., Albrecht T. R., Quate C. F.* // Appl. Phys. Lett. 1989. Vol. 54. P. 2651 https://doi.org/10.1063/1.101024
21. *VanLandingham M.R, McKnight S. H. et al.* // J. Adhesion. Adhesion. 1997. Vol. 64. P. 31.
22. *Sneddon I. N.* // Int. J. Eng. Sci. 1965. 3. P. 47. https://doi.org/10.1016/0020–7225(65)90019–4
23. *Smith J. R. Swift J. A.* // Micron. 2005. Vol. 36. P. 261. https://doi.org/10.10116.j.micron.2004.11.004
24. *Smith J. R., Tsibouklis J., Nevel T. G., Breakspear S.* // Appl. Surf. Sci. 2013. Vol. 285. Pt B. P. 638. https://doi.org/10.1016/j.apsusc.2013.08.104
25. *Rogers G.* // Cosmet. Sci. 2013. Vol. 6. No. 2. P. 32 https://doi.org/10.3390/cosmetics6020032
26. *Mcmullen R. L., Zhang G.* // J. Cosmet. Sci. 2020. Vol. 71. P. 117.
27. *Belikov S., Erina N., Huang L. et al.* // J. Vac. Vac. Sci. Tech. B. 2009. Vol. 27. P. 984. https://doi.org/10.1017/S1431927616002622
28. *Parbhu A., Bryson W., Lal R.* // Biochemistry. 1999. Vol. 38. P. 11755. https://doi.org/10.1021/bi990746d
29. Aebi U., Fowler W. E., *Rew P, Sun T-T.* // J. Cell Biology. 1983. Vol. 97. P. 1131. https://doi.org/10.1083/JCB.97.4.1131
30. *Ezawa Y., Nagase S., Mamada A. et al.* // Cosmetics. 2019. Vol. 6. P. 24. https://doi.org/10.3390/cosmetics6020024